JACS
JOURNAL OF THE AMERICAN CHEMICAL SOCIETY
Article
pubs.acs.org/JACS

Understanding the Effect of Monomeric Iridium(III/IV) Aquo Complexes on the Photoelectrochemistry of $IrO_x{\cdot}nH_2O$-Catalyzed Water-Splitting Systems

Yixin Zhao,[†,⊥] Nella M. Vargas-Barbosa,[‡,⊥] Megan E. Strayer,[‡] Nicholas S. McCool,[‡] Maria-Erini Pandelia,[‡] Timothy P. Saunders,[‡,¶] John R. Swierk,[‡,§] Juan F. Callejas,[‡] Lasse Jensen,*[,‡] and Thomas E. Mallouk*[,‡,§,∥]

[†]School of Environmental Science and Engineering, Shanghai Jiao Tong University, 800 Dongchuan Road, Shanghai 200240, China
[‡]Department of Chemistry, [§]Department of Biochemistry and Molecular Biology, and [∥]Department of Physics, The Pennsylvania State University, University Park, Pennsylvania 16802, United States

Supporting Information

ABSTRACT: Soluble, monomeric Ir(III/IV) complexes strongly affect the photoelectrochemical performance of $IrO_x{\cdot}nH_2O$-catalyzed photoanodes for the oxygen evolution reaction (OER). The synthesis of $IrO_x{\cdot}nH_2O$ colloids by alkaline hydrolysis of Ir(III) or Ir(IV) salts proceeds through monomeric intermediates that were characterized using electrochemical and spectroscopic methods and modeled in TDDFT calculations. In air-saturated solutions, the monomers exist in a mixture of Ir(III) and Ir(IV) oxidation states, where the most likely formulations at pH 13 are $[Ir(OH)_5(H_2O)]^{2-}$ and $[Ir(OH)_6]^{2-}$, respectively. These monomeric anions strongly adsorb onto $IrO_x{\cdot}nH_2O$ colloids but can be removed by precipitation of the colloids with isopropanol. The monomeric anions strongly adsorb onto TiO_2, and they promote the adsorption of ligand-free $IrO_x{\cdot}nH_2O$ colloids onto mesoporous titania photoanodes. However, the reversible adsorption/desorption of electroactive monomers effectively short-circuits the photoanode redox cycle and thus dramatically degrades the photoelectrochemical performance of the cell. The growth of a dense TiO_2 barrier layer prevents access of soluble monomeric anions to the interface between the oxide semiconductor and the electrode back contact (a fluorinated tin oxide transparent conductor) and leads to improved photoanode performance. Purified $IrO_x{\cdot}nH_2O$ colloids, which contain no adsorbed monomer, give improved performance at the same electrodes. These results explain earlier observations that $IrO_x{\cdot}nH_2O$ catalysts can dramatically degrade the performance of metal oxide photoanodes for the OER reaction.

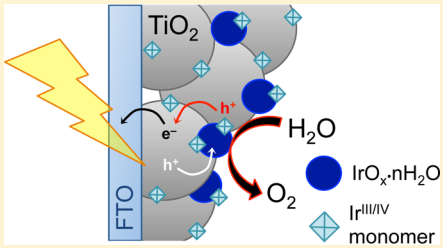

INTRODUCTION

Photoelectrochemical cells (PECs) utilize sunlight to drive electrochemical reactions. In solar fuel applications of PECs, the anode reaction is typically the oxygen evolution reaction (OER). The efficiency of PECs is strongly dependent on efficient catalysis of the OER because of the complex four-electron, four-proton mechanism of the reaction. Many catalysts have been studied including those based on precious metals[1−7] and earth-abundant elements.[8−14] The incorporation of these catalysts into photoabsorbers and onto the surfaces of oxide semiconductors has been well studied.[15−21]

Iridium oxide is a highly active OER catalyst and has been recently benchmarked by McCrory et al. as the only known solid electrocatalyst for the OER that is highly active and stable in acidic electrolytes.[12] The overpotential for water oxidation at iridium oxide is low over a broad range of pH,[1] although it is less active and unstable under strongly alkaline conditions. Amorphous iridium oxide nanoparticles ($IrO_x{\cdot}nH_2O$) have been used successfully to improve the OER efficiency of both PECs[15,22,23] and molecular photochemical systems.[24,25]

Recently, Bard and co-workers used scanning electrochemical microscopy to probe the photoelectrochemical activity of n-type $BiVO_4$.[26,27] In characterizing the effects of metal and metal oxide electrocatalysts on tungsten-doped $BiVO_4$ photoanodes, they found rather surprisingly that the photocurrent was dramatically reduced by incorporating $IrO_x{\cdot}nH_2O$ into the photoelectrode, whereas other catalysts such as cobalt oxide increased the photocurrent.

Alkaline hydrolysis of Ir(III) or Ir(IV) salts produces a soluble intermediate that condenses in acid to form catalytically active, ligand-free $IrO_x{\cdot}nH_2O$ nanoparticles.[2] In this preparation of $IrO_x{\cdot}nH_2O$ colloids, there are distinct features in UV−vis spectra that suggest the presence of a low nuclearity and possibly monomeric anion. A strong absorption band centered at 313 nm is observed, most likely from a ligand-to-metal charge transfer absorption of a hydroxyiridate species. At concentrations below about 0.5 mM, no visible absorption bands are observable and there is minimal light scattering by the solution. At higher concentrations, a weak 580 nm band appears along with light scattering that is typical of blue $IrO_x{\cdot}nH_2O$ colloids. Both absorption features are pH-dependent,

Received: April 2, 2015
Published: June 24, 2015

DOI: 10.1021/jacs.5b03470
J. Am. Chem. Soc. 2015, 137, 8749−8757

and the 313 nm absorbance is strong in very basic solutions. This suggests a reversible acid condensation of the hydroxyiridate monomer to form $IrO_x{\cdot}nH_2O$ colloids.

We report here a systematic spectroscopic, electrochemical, and computational study to identify the monomeric iridium complexes formed in this reaction. Interestingly, we find that these anions adsorb strongly not only to ligand-free $IrO_x{\cdot}nH_2O$ colloids but also to TiO_2 and other oxide semiconductor surfaces. The adsorption−desorption equilibrium of these previously unrecognized electroactive anions significantly complicates the photoelectrochemistry of oxide photoanodes that are functionalized with $IrO_x{\cdot}nH_2O$ catalyst particles. By removal of the monomer, blocking of its path to the electrode back contact, or use of alternative attachment chemistries for the $IrO_x{\cdot}nH_2O$ colloids, the photoelectrochemical performance of these catalyzed electrodes is dramatically improved.

EXPERIMENTAL SECTION

Low-Temperature Ligand-Free $IrO_x{\cdot}nH_2O$ Nanoparticle Synthesis. K_2IrCl_6 (0.2 mmol) was dissolved in 90 mL of 8 mM aqueous NaOH. The solution was heated rapidly to 75 °C with strong stirring. The solution was immediately cooled in an ice bath where it remained stirring for ca. 64 h. The pH was closely monitored and maintained at 11.9 by addition of 1 M NaOH throughout the reaction. The final solution volume was adjusted to 100 mL with nanopure water. The colloidal solutions prepared by this low-temperature method are denoted herein as LT-$IrO_x{\cdot}nH_2O$. For comparison purposes, ligand-free $IrO_x{\cdot}nH_2O$ nanoparticles reported by Murray and co-workers[1] were also synthesized and are referred to as LF-$IrO_x{\cdot}nH_2O$. Separation of adsorbed anionic hydroxyiridate monomers from both kinds of ligand-free colloidal particles was accomplished by precipitating the colloids in double the volume of isopropanol and then redispersing in the desired solvent. The precipitated colloids can be redispersed in nanopure water, DMSO, THF, and DMF.

Ligand-Capped $IrO_x{\cdot}nH_2O$ Nanoparticle Synthesis. 2-Carboxyethylphosphonic acid (PCOOH)-capped $IrO_x{\cdot}nH_2O$ nanoparticles were synthesized as previously described.[28] Briefly, 0.3 mmol of PCOOH and 0.05 mmol of K_2IrCl_6 were dissolved in 50 mL of nanopure water, and the pH was adjusted to 5.0 with concentrated NaOH. The solution was refluxed at 90 °C for 1 h and turned colorless. The solution was allowed to cool to 80 °C, and the pH was monitored and adjusted to 7.5 until the solution turned clear blue and the absorbance peak at ca. 580 nm was stable (ca. 8 h). The nanoparticles were purified to remove excess ligand and hydroxyiridate monomers using a DOWEX 1X8-50 anion exchange resin that was pretreated with NaOH for 10 min and washed until neutral with nanopure water.

Hydroxyiridate Monomer Solution Synthesis. One millimolar solutions of hydroxyiridate monomers were prepared by alkaline hydrolysis of K_2IrCl_6 solutions[29] and were diluted to the appropriate concentrations for adsorption experiments. To prepare 100 μM solutions, 0.005 mmol K_2IrCl_6 was dissolved in 50 mL of standardized 0.1008 M aqueous NaOH and heated to 70 °C until colorless, clear solutions were obtained. The solution was immediately cooled in an ice bath and kept in a refrigerator at 2 °C until used.

Photoanode Preparation. Mesoporous TiO_2 electrodes were prepared by doctor-blading anatase TiO_2 paste directly onto fluorine-doped tin oxide (FTO)-coated glass slides masked with three layers of Scotch tape (ca. 10 μm total thickness). These mesoporous anatase electrodes and rutile-TiO_2 vertical nanorod electrodes were prepared following previously published procedures.[30,31] Tungsten-doped bismuth vanadate electrodes were prepared as described by Bard and co-workers.[27]

TDDFT Methodology. All calculations were performed using a local version of the Amsterdam Density Functional (ADF) program package.[32−34] The geometries were optimized using a TZ2P basis set and the OPBE functional. The OPBE functional was chosen because it has been shown to provide a good description of spin-states.[35] Solvent effects were accounted for using COSMO,[36] and scalar relativistic effects were included using the zeroth-order regular approximation (ZORA).[37,38] Excitation energies were calculated using the long-range corrected LCY-BP86 functional based on the Yukawa potential with a range separation parameter of 0.34.[39]

Measurements and Characterization. Electrochemical measurements and colloid deposition on glassy carbon (GC) rotating disk electrodes (RDEs) were performed with a BAS 100B electrochemical workstation. Photoelectrochemical measurements were made using a 150 mW Xe lamp with AM1.5 filter in a quartz cell that enabled illumination from the back side (i.e., through the glass/FTO contact) of semiconductor electrodes, using a Ag/AgCl/saturated KCl reference electrode. UV−vis spectra were recorded on a Varian Cary 6000i spectrophotometer.

Spectroelectrochemical experiments were performed using a Honeycomb quartz cell (Pine Research Instruments) with gold honeycomb working and counter electrodes and a homemade standard calomel electrode (SCE). SCE was used instead of Ag/AgCl as the reference electrode because of the long time scale and high pH conditions of these experiments. The dimensions of the cell and the diffusivity of electroactive species determined the time needed to aquire the spectrum after each potential step. The diffusion time scale (τ) in a spectroelectrochemical cell is given by eq 1:

$$\tau = \delta^2/(2D) \quad (1)$$

Here δ (cm) is the longest distance that electroactive species have to travel to reach the electrode surface in the honeycomb working electrode and D is the diffusion coefficient (cm^2/s). In our experiments, δ was 0.05 cm, the width of the honeycomb channels, and D was estimated as 5×10^{-6} cm^2/s, so τ was about 250 s. UV−vis spectra were collected approximately 30 min after each potential step in order to ensure adequate time for diffusion of oxidized and reduced monomeric anions.

Transmission electron microscopy (TEM) images were obtained using a JEOL JM-2010 microscope with a LaB_6 electron source at an accelerating voltage of 200 keV. Samples were prepared by dropping the solution onto a lacey carbon-coated copper grid. The samples were dried at room temperature before use. EPR measurements were carried out at cryogenic temperatures on a Bruker ESP300 CW X-band spectrometer (operating at approximately 9.48 GHz) equipped with a rectangular cavity (TE102) and a continuous-flow cryostat (Oxford 910) with a temperature controller (Oxford ITC 503). The EPR spectrum of the monomer solution was obtained after subtraction of a 0.1 M NaOH solution spectrum. Spin quantitation was performed relative to a 256.25 μM Cu^{2+}-EDTA standard.

RESULTS AND DISCUSSION

Characterization of Hydroxyiridate Anions. Although the alkaline hydrolysis of K_2IrCl_6 can produce stable, catalytically active $IrO_x{\cdot}nH_2O$ nanoparticle suspensions, the yield is limited by an equilibrium between small molecule, anionic intermediates and the colloid at a given pH.[2] The soluble, colorless Ir-containing anions formed in base can be converted to deep blue iridium oxide colloids by an acidic condensation reaction that can be monitored by UV−vis spectroscopy. As the pH is lowered, the UV band at 313−318 nm decreases and the visible $IrO_x{\cdot}nH_2O$ band centered at 580 nm increases. In earlier papers, the colorless hydroxyiridate anion has been described as an Ir(IV) anion or as $[Ir(OH)_6]^{2-}$,[2,29,40,41] although some reports have suggested that it is an Ir(III) complex.[42,43]

A linear Beer's law plot of these solutions at concentrations between 0.002 and 0.10 mM (Figure 1A) establishes that the nuclearity of Ir complexes contributing to the 318 nm band does not change over this concentration range and that the solution most likely contains monomeric complexes.

DOI: 10.1021/jacs.5b03470
J. Am. Chem. Soc. 2015, 137, 8749−8757

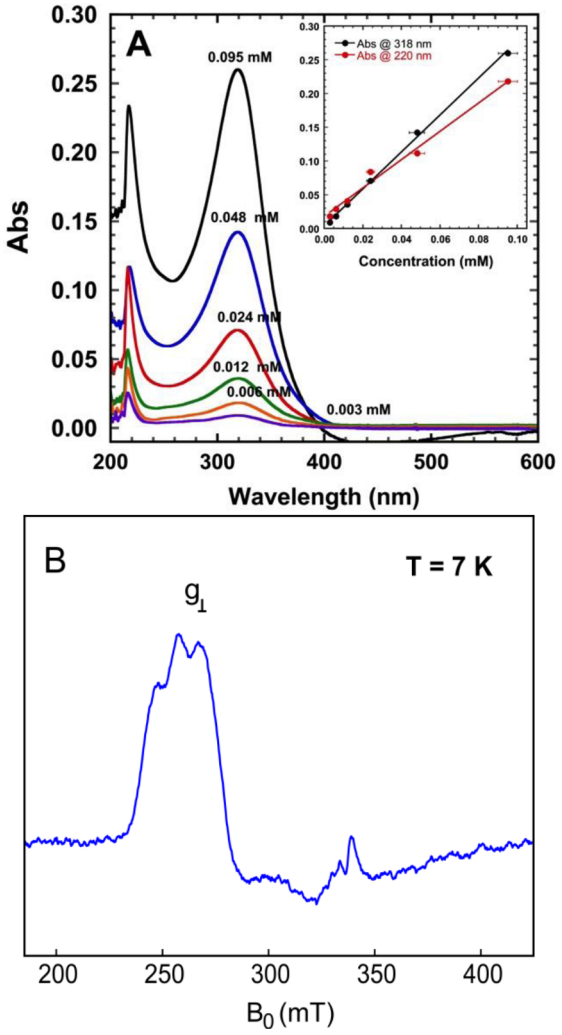

Figure 1. (A) UV−vis spectra of solutions prepared by hydrolysis of K_2IrCl_6 in air-saturated 0.1 M NaOH. Inset shows a Beer's law plot of the absorbance at 220 and 318 nm. (B) EPR spectrum of a frozen 0.13 mM Ir solution prepared under the same conditions as in part A and recorded at 7 K. Microwave frequency = 9.480 GHz, modulation amplitude 1 mT, microwave power 2 mW.

Electron paramagnetic resonance (EPR) experiments were performed on frozen solutions of the monomer to quantify the amount of paramagnetic Ir^{IV}. Figure 1B shows the EPR spectrum, which exhibits an almost axial signal characteristic of a low-spin (S = 1/2) d^5 iridium(IV) hydroxo/aqua coordinate complexes.[44] The EPR signal exhibits complex features that may originate from the interaction of the unpaired electron with the iridium nucleus (Ir has two magnetic isotopes with I = 3/2 in a 2:1 ratio) or with nearby strongly coupled nuclei (e.g., ^1H). Spin quantitation of the Ir^{IV} complex yields 0.04 mM from a solution originally containing 0.13 mM K_2IrCl_6. This suggests that the majority (ca. 70%) of Ir in the solution exists in the EPR-silent (d^6, S = 0) +3 oxidation state. We note that this is consistent with redox titrations of blue $IrO_x{\cdot}nH_2O$ colloids, which show an average oxidation state of 3.2.[40]

Cyclic voltammetry (CV) of these solutions at 0.10 mM concentration, where the monomer is stable, helps to explain the mixture of oxidation states formed in the hydrolysis reaction. Figure 2 shows a CV at pH 13 on a glassy carbon electrode. There are two reversible one-electron redox

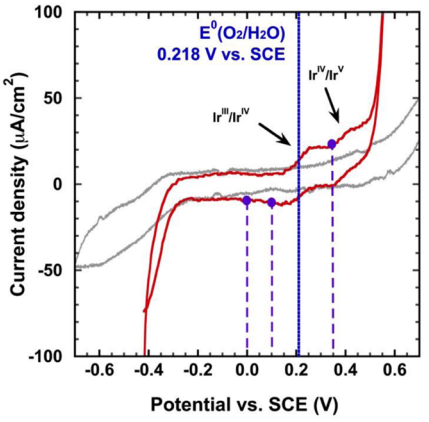

Figure 2. Cyclic voltammogram (red trace) of 0.10 mM hydroxyiridate(III/IV) in unstirred, air-saturated 0.1 M NaOH on a glassy carbon electrode at 10 mV/s. The gray trace is the clean glassy carbon electrode background current in 0.1 M NaOH. The dashed blue line indicates the formal potential of the oxygen/water couple at pH 13. The purple dots and lines indicate the potentials selected for the spectroelectrochemical experiments in Figure 3.

processes that can be ascribed to Ir^{III}/Ir^{IV} and Ir^{IV}/Ir^{V} interconversions. The onset of high anodic current at potentials positive of +0.55 V vs SCE is attributed to the oxygen evolution reaction (OER) (η_{OER} = 330 mV at 100 $\mu A/cm^2$). In this solution, the formal potential of the Ir^{III}/Ir^{IV} couple is approximately coincident with the potential of the oxygen/water couple. This is consistent with the 30% yield of the Ir(IV) monomeric species detected by EPR and with earlier observations that the synthesis of $IrO_x{\cdot}nH_2O$ colloids from either Ir(IV) or Ir(III) involves an Ir(III) intermediate.[45−47]

We attempted to measure the charge on the Ir(III) complex by the ion exchange method of Cady and Connick.[48] Unfortunately, the monomeric anions are stable only at low concentration (<0.5 mM) in strong base (0.1 M NaOH), so these attempts were unsuccessful. Spectroelectrochemical experiments were then carried out to establish the contributions of Ir(III) and Ir(IV) anions to the spectral features shown in Figure 1 and to identify the species present in each oxidation state.

Figure 3A−C shows the changes in the spectra as a function of time under controlled-potential conditions, at +350 mV vs SCE for conversion of Ir^{III} to Ir^{IV}, and potentials at or negative of +100 mV vs SCE for the conversion of Ir^{IV} to Ir^{III}. When a +350 mV vs SCE bias is applied ($Ir^{III} \rightarrow Ir^{IV}$), the peak centered at 318 nm broadens and the absorbance decreases (Figure 3A). At the same time, the intensity of the peak centered at 220 nm increases dramatically. When the bias is shifted to +100 mV vs SCE ($Ir^{IV} \rightarrow Ir^{III}$), the 318 nm peak becomes narrower and similar in shape to that of the original spectrum within 30 min (Figure 3A). A slight blue shift occurs, and λ_{max} is then centered at 313 nm. At the same time, the peak centered at 220 nm decreases in intensity. As the electrolysis progresses at +100 mV and 0 mV vs SCE, the peak centered at 313 nm continues to increase but does not recover to the absorbance value of the original spectrum. Under these conditions, the absorbance at 220 nm increases, albeit at a slower rate than at +350 mV vs SCE. This is most likely a consequence of light scattering because of irreversible colloid formation, because it is more pronounced at shorter wavelengths and longer time scales. At the end of the experiment, the potential was returned to +350

DOI: 10.1021/jacs.5b03470
J. Am. Chem. Soc. 2015, 137, 8749−8757

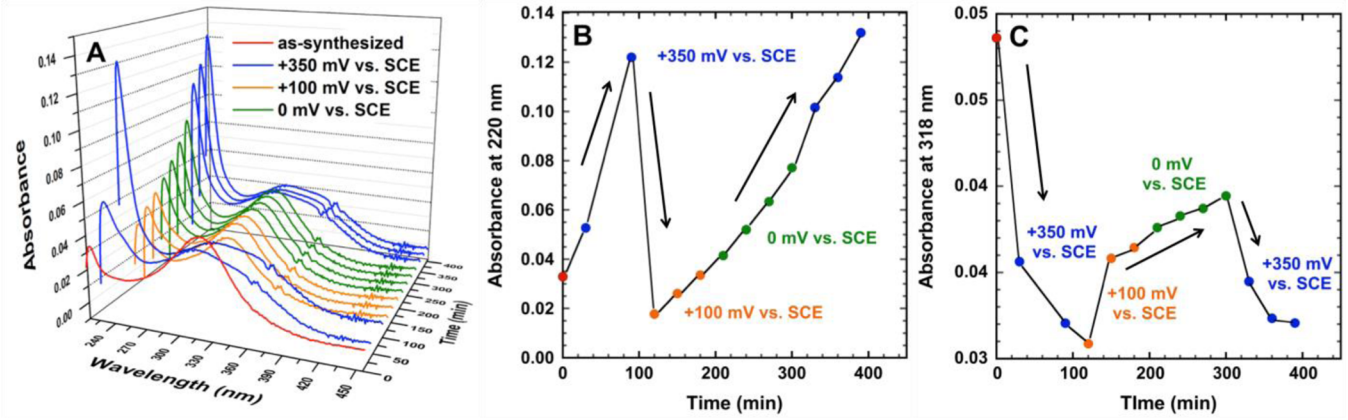

Figure 3. (A) Controlled-potential spectroelectrochemistry of 0.10 mM hydroxyiridate(III/IV) solutions. (B, C) Time- and potential-dependent absorptivity changes for the peaks centered at 220 and 318 nm, respectively. The spectral changes of the peak centered at 220 nm is consistent with the formation of Ir^{IV} at +350 mV. The peak centered at 318 nm is a combination of transitions corresponding to Ir^{III} and Ir^{IV} species.

mV vs SCE ($Ir^{III} \rightarrow Ir^{IV}$, Figure 3A, second set of blue traces). As observed on the first excursion to positive potential, the peak in the 313−318 nm range broadened and decreased in intensity and the peak centered at 220 nm increased rapidly.

Taken together the potential-dependent spectra suggest that the absorbance at 220 nm is predominantly from an Ir^{IV} species and that the 318 nm band is a combination of both Ir^{III} and Ir^{IV} species. The time-dependent absorbance values at 220 and 318 nm as a function of the applied potential are summarized in Figure 3B,C. Complete spectroelectrochemical plots are shown in Figure S1 of the Supporting Information.

TDDFT calculations were performed to correlate the results of the spectro-electrochemical and EPR experiments with specific structures and Ir oxidation states. In order to validate the TDDFT method, calculations were first done for the complexes $[IrCl_6]^{3-}$ and $[Ir(H_2O)_6]^{3+}$ to validate the method. Table S1, Supporting Information, summarizes the calculated energies of the d−d transitions, which demonstrate a good agreement between the experimental and modeled spectra.[43,49]

The extinction coefficient of the hydroxyiridate anion at 318 nm was determined earlier to be ca. 3300 M^{-1} cm^{-1},[2] which suggests a ligand-to-metal charge transfer (LMCT) absorption. Simulated spectra of possible Ir^{III} and Ir^{IV} anions are shown in Figure S2, Supporting Information. The calculated spectra are in good agreement with the assignment of the 220 nm band to an Ir^{IV} anion, namely, $Ir^{IV}(OH)_6^{2-}$. However, the transition at 318 nm cannot be as clearly assigned to a single anion. Both $Ir^{IV}(OH)_6^{2-}$ and $Ir^{III}(OH)_6(H_2O)^{2-}$ have calculated absorption bands in the 300−400 nm region, whereas the low symmetry of the latter complex further complicates the calculation of extinction coefficients. However, the more symmetric $Ir^{III}(OH)_6^{3-}$ anion has very little calculated absorbance at wavelengths longer than 300 nm. Taken together with the EPR results, this suggests that the predominant molecular structure of the Ir(III) species in air-saturated solutions at pH 13 is the $Ir^{III}(OH)_5(H_2O)^{2-}$ anion. Alkaline hydrolysis of $IrCl_6^{2-}$ thus produces a mixture of Ir(III) and Ir(IV) monomers as the dianions $Ir^{III}(OH)_5(H_2O)^{2-}$ and $Ir^{IV}(OH)_6^{2-}$.

As-Synthesized and Purified Ligand-free $IrO_x{\cdot}nH_2O$ Nanoparticles. The monomeric Ir(III/IV) anions could be separated from $IrO_x{\cdot}nH_2O$ nanoparticles by precipitating the colloids with isopropanol and then resuspending them in polar solvents. This was confirmed by the disappearance of the absorption peak at 313 nm (Figure 4A). The scattering background increases when the precipitated colloids are resuspended, suggesting that the flocculation of the colloids is not completely reversible. Analysis of TEM images shows that the diameter of the primary nanoparticles remains the same within experimental error, 1.4 ± 0.3 and 1.2 ± 0.3 nm before and after purification, respectively (Figures 4B,C).

In order to determine the effect of the monomeric anions on the electrocatalytic activity of $IrO_x{\cdot}nH_2O$ nanoparticles, the colloidal solutions were studied as dispersed redox catalysts at a glassy carbon rotating disk electrode. Figure 4D shows voltammetry of these nanoparticle solutions at pH 13. The LF-$IrO_x{\cdot}nH_2O$ (Figure 4D, red trace) shows the highest electrocatalytic activity, while the LT-$IrO_x{\cdot}nH_2O$ nanoparticles (Figure 4D, purple trace) are moderately active. After purification of LT-$IrO_x{\cdot}nH_2O$, that is, removal of the monomeric anions, the apparent catalytic activity is substantially diminished (Figure 4D, blue trace). In this experiment, PCOOH-capped $IrO_x{\cdot}nH_2O$ nanoparticles exhibited the lowest electrocatalytic activity, possibly due to slow electron transfer to the electrode through the capping ligands (Figure 4D, green trace).

The difference in electrocatalytic activities of the nanoparticle solutions is most likely related to the presence (or absence) of monomeric Ir(III/IV) anions. Since these anions are a precursor to the formation of $IrO_x{\cdot}nH_2O$ nanoparticles, under anodic bias, that is, conditions where OER catalysis occurs, the local decrease in pH can cause the monomer to condense to catalytically active $IrO_x{\cdot}nH_2O$ nanoparticles on the electrode surface. The *in situ* formation of $IrO_x{\cdot}nH_2O$ nanoparticles on the electrode can result in the observed high catalytic currents. The inset in Figure 4D shows the color of the $IrO_x{\cdot}nH_2O$ colloidal solutions tested. The lack of blue color in solution 1 (LF-$IrO_x{\cdot}nH_2O$), which shows the highest catalytic activity, indicates a low concentration of colloidal $IrO_x{\cdot}nH_2O$ relative to the colorless monomeric anions. Solution 2 (LT-$IrO_x{\cdot}nH_2O$) has a deeper blue color, that is, a predominance of colloidal $IrO_x{\cdot}nH_2O$ relative to monomer. The increased concentration of colloidal $IrO_x{\cdot}nH_2O$ in this case is most likely due to the longer time allowed for the slow hydrolysis reaction to proceed.

$IrO_x{\cdot}nH_2O$ Nanoparticle-Modified Photoelectrodes. TiO_2 electrodes soaked in PCOOH-capped $IrO_x{\cdot}nH_2O$ colloidal solutions show effective deposition of $IrO_x{\cdot}nH_2O$ nanoparticles. This same procedure was followed with the as-synthesized and purified LT-$IrO_x{\cdot}nH_2O$ colloids. Figure 5

DOI: 10.1021/jacs.5b03470
J. Am. Chem. Soc. 2015, 137, 8749−8757

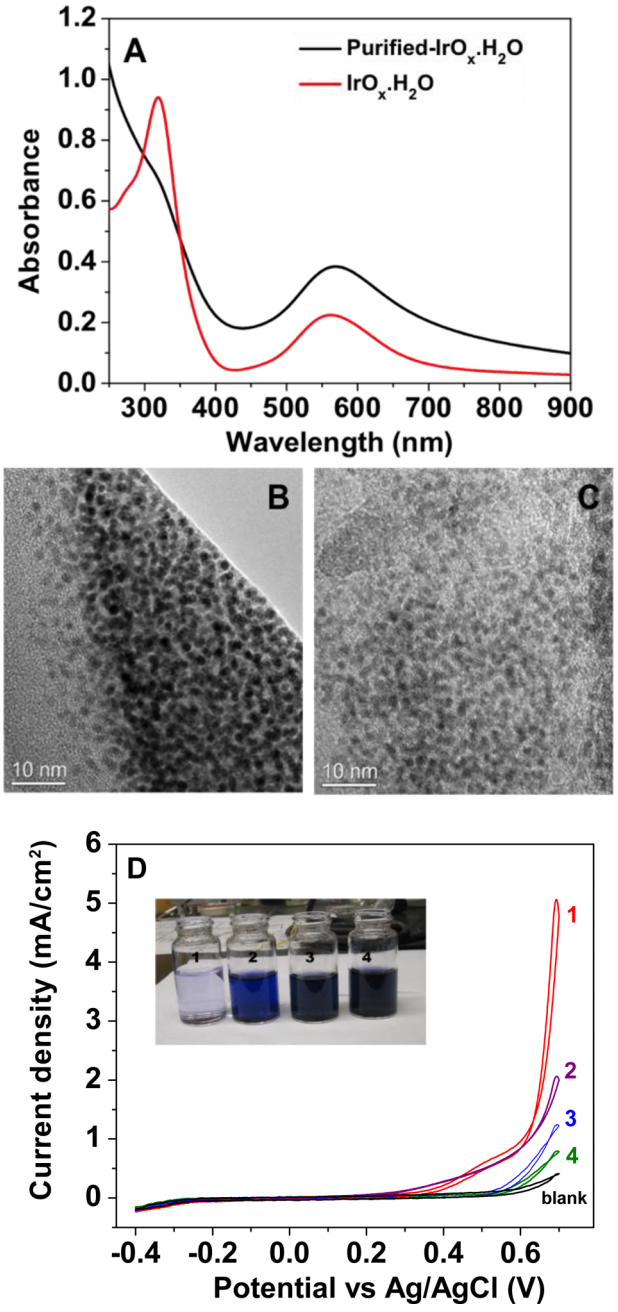

Figure 4. (A) UV−vis spectra and transmission electron micrographs of (B) as-synthesized and (C) purified LT-IrO$_x$·nH$_2$O. The average particle diameters were 1.4 ± 0.3 nm [n = 139] and 1.2 ± 0.3 nm [n = 125] for the as-synthesized and purified colloidal samples, respectively. (D) Cyclic voltammograms of deaerated 1 mM (based on total Ir) nanoparticle solutions at pH 13: (1) LF-IrO$_x$·nH$_2$O, (2) as-synthesized LT-IrO$_x$·nH$_2$O, (3) purified LT-IrO$_x$·nH$_2$O, and (4) PCOOH-capped IrO$_x$·nH$_2$O. All CVs were taken at 20 mV/s using a glassy carbon rotating disk electrode (blank) at a rotation rate of 600 rpm in a pH 13 NaOH solution. Significant differences in the electrocatalytic activity of the colloids as dissolved redox catalysts are observed. The inset picture shows the IrO$_x$·nH$_2$O solutions used.

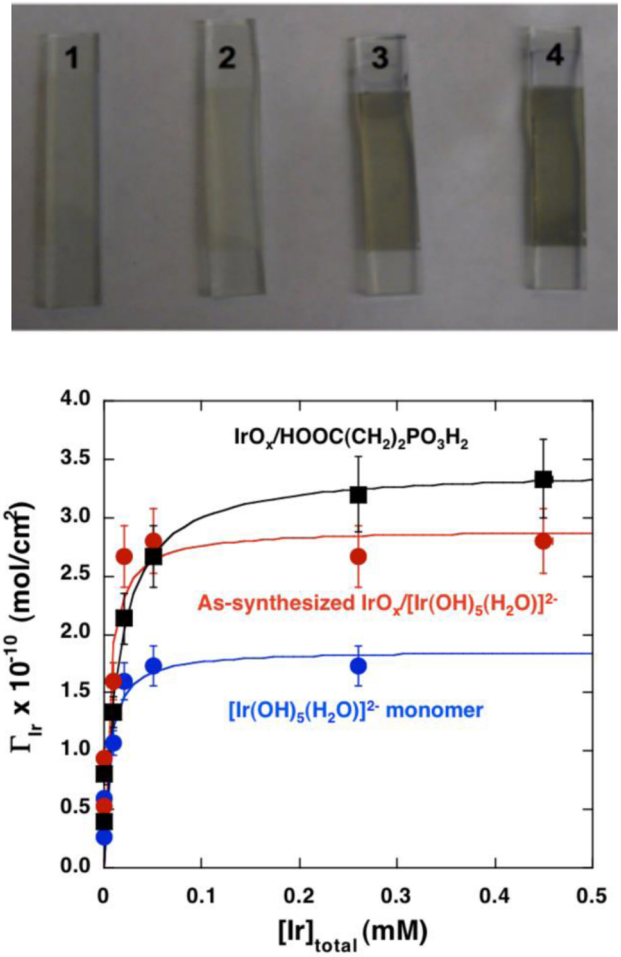

Figure 5. (top) Photographs of mesoporous TiO$_2$ slides: (1) bare TiO$_2$, (2) soaked in purified LT-IrO$_x$·nH$_2$O, (3) soaked in PCOOH-capped IrO$_x$·nH$_2$O, and (4) soaked in as-synthesized LT-IrO$_x$·nH$_2$O colloidal solution. (bottom) Adsorption isotherms of iridium-based solutions: (blue) monomer solution, (red) as-synthesized LT-IrO$_x$·nH$_2$O, (black) purified PCOOH-capped IrO$_x$·nH$_2$O. Fit lines represent Langmuir adsorption isotherms.

compares a bare mesoporous TiO$_2$ slide (slide 1) with postdeposition slides of purified LT-IrO$_x$·nH$_2$O, PCOOH-capped IrO$_x$·nH$_2$O, and as-synthesized LT-IrO$_x$·nH$_2$O (slides 2−4, respectively). The lack of color on slide 2 demonstrates that there is little or no adsorption of LT-IrO$_x$·nH$_2$O particles when the purified colloid solution (free of monomeric Ir^{III}(OH)$_5$(H$_2$O)$^{2-}$ and Ir^{IV}(OH)$_6^{2-}$) was used. However, slides immersed in PCOOH-capped and as-synthesized LT-IrO$_x$·nH$_2$O colloidal solutions show significant deposition of the nanoparticles (slides 3 and 4, respectively). These results highlight the necessity of an anchoring group to attach colloidal IrO$_x$·nH$_2$O particles to the TiO$_2$ surface. For the ligand-capped IrO$_x$·nH$_2$O, PCOOH can act as the anchoring group. For as-synthesized LT-IrO$_x$·nH$_2$O, the adsorbed monomeric anions apparently anchor the colloids to the TiO$_2$ surface. ζ-Potential measurements indicate that as-synthesized and purified LT-IrO$_x$·nH$_2$O, as well PCOOH-capped IrO$_x$·nH$_2$O, have the same ζ-potential (at pH 12, −25 ± 5 mV) within experimental error. This suggests that electrostatic factors do not differentiate purified LT-IrO$_x$·nH$_2$O from the other colloids and points to the capping/stabilizing behavior of the adsorbed monomeric anions.

To quantify the coverage (Γ) of iridium oxide nanoparticles and monomeric anions on the photoanodes, adsorption isotherms were measured (Figure 5). Ten micrometer thick mesoporous TiO$_2$ electrodes (3 cm^2 area) were soaked overnight in different concentrations of the Ir-containing solutions. Isotherms were obtained by monitoring the

DOI: 10.1021/jacs.5b03470
J. Am. Chem. Soc. 2015, 137, 8749−8757

absorption band of the colloids at 580 nm and the monomer at 313 nm, and coverages were calculated on a per mole Ir (not per particle) basis, assuming a roughness factor of 1000 for the TiO_2 films. All systems studied could be modeled with Langmuirian adsorption behavior, as shown in Figure 5. The PCOOH-capped $IrO_x{\cdot}nH_2O$ showed the highest saturation coverage (3.4×10^{-10} mol/cm^2) followed by as-synthesized LT-$IrO_x{\cdot}nH_2O$ and monomer solutions, which gave saturation coverages of 2.9×10^{-10} and 1.9×10^{-10} mol/cm^2, respectively. The latter corresponds to approximately monolayer coverage of monomer on the TiO_2 surface. The values of the equilibrium constants were 72, 190, and 180 mM^{-1}, respectively, indicating especially strong binding of the monomer and the monomer-capped colloids to the TiO_2 surface. Since little adsorption of $IrO_x{\cdot}nH_2O$ nanoparticles was observed when the colloids were purified to remove the monomeric anions, it can be concluded that the anions play a key role in the deposition of $IrO_x{\cdot}nH_2O$ onto mesoporous TiO_2 electrodes.

Photoelectrochemistry. Recently, Bard and co-workers tested the effects of various OER catalysts on tungsten-doped bismuth vanadate photoanodes using scanning electrochemical microscopy.[27] They determined that despite having excellent electrocatalytic activity for OER, iridium oxide performed poorly as a cocatalyst in comparison to cobalt oxide and platinum for photoelectrochemical water oxidation. In contrast, a report by Grätzel and co-workers showed that electrodeposited iridium oxide on nanostructured hematite electrodes resulted in a significant performance enhancement for the photoelectrochemical OER.[15] We can now consider these seemingly inconsistent results in light of the likely presence of adsorbed monomeric Ir(III) and Ir(IV) anions and their electrochemical reactions.

Slow linear sweep voltammetry (LSV) under intermittent AM1.5 illumination was used to characterize the photoresponse of metal oxide photoanodes in the absence and presence of monomeric Ir(III/IV) anions and $IrO_x{\cdot}nH_2O$ catalyst particles. In Figure 6A, uncatalyzed mesoporous anatase photoelectrodes show the expected photoresponse at positive potentials, with photocurrents of ~0.04 mA/cm^2 corresponding to the UV light-driven OER. The photocurrent of these electrodes was dramatically diminished (by ca. 75%) when the electrode was exposed to a 10 μM solution of the Ir(III/IV) monomer for 10 s (Figure 6A, blue trace). The same TiO_2 electrode was modified with $IrO_x{\cdot}nH_2O$ nanoparticles by immersion in a 2 mM as-synthesized LT-$IrO_x{\cdot}nH_2O$ solution (Figure 6A, red trace). In this case, the photocurrent is even further diminished, although there is a significant increase in the dark current at high overpotential due to electrocatalysis of the dark OER (Figure 6A, red trace). The presence of the monomeric Ir(III/IV) anions is detrimental to PECs that utilize $IrO_x{\cdot}nH_2O$ as the OER catalyst, most likely because these electroactive anions can desorb and mediate charge recombination at the interface between the FTO back contact and the mesoporous TiO_2 film, as illustrated in Scheme 1.

Bard and co-workers have recently demonstrated that blocking the FTO back contact with electrodeposited amorphous TiO_2 dramatically improves the performance of $BiVO_4$ photoelectrodes.[50] Grätzel and co-workers created a similarly dense layer in the preparation of their hematite electrodes, which were later modified with colloidal iridium oxide.[15]

Here, we prepared a thin (ca. 25 nm thick) TiO_2 underlayer by spray pyrolysis of 0.2 M Ti(IV) bis(ethyl acetoacetate)-diisopropoxide 1-butanol solution at 450 °C, onto which we deposited the mesoporous TiO_2 film. The photoelectrochemistry of these electrodes was tested under the same conditions as those without the dense TiO_2 underlayer. In this case, the

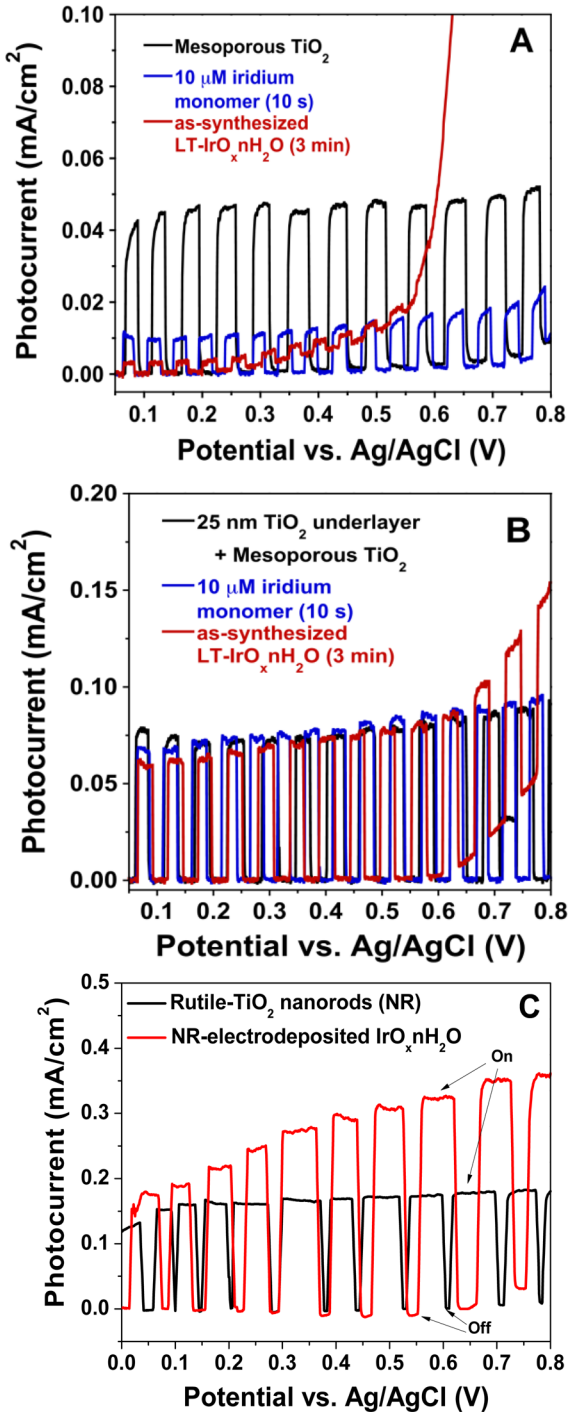

Figure 6. Linear sweep voltammograms (LSV) at 5 mV/s in 0.1 M NaOH under AM1.5 irradiation of (A) bare mesoporous TiO_2 electrode (black), mesoporous TiO_2 electrode soaked in 10 μM iridium hydroxide solution for 10 s (blue), and mesoporous TiO_2 electrode soaked in 2 mM LT-$IrO_x{\cdot}nH_2O$ for 3 min (red), (B) mesoporous TiO_2 electrode with a 25 nm TiO_2 underlayer (black), same electrode soaked in 10 μM iridium hydroxide solution for 10 s (blue), and same electrode soaked in 2 mM LT-$IrO_x{\cdot}nH_2O$ for 3 min (red), and (C) bare rutile-TiO_2 nanorod (NR) film (black) and $IrO_x{\cdot}nH_2O$-modified through electrodeposition of Ir(III/IV) (red).

DOI: 10.1021/jacs.5b03470
J. Am. Chem. Soc. 2015, 137, 8749−8757

Scheme 1. Cartoon Representation of the Short-Circuiting of a TiO_2 Water Splitting Anode by Adsorption/Desorption of Electroactive Hydroxyiridate Anions[a]

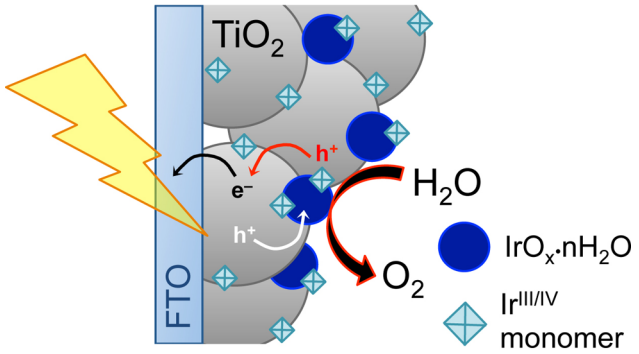

[a]Photogenerated holes are scavenged by the Ir^{III} form of the complex, converting it to Ir^{IV}. The oxidized complex desorbs and is reduced back to Ir^{III} by trapped electrons at the interface between the TiO_2 film and the FTO back contact. Covering the FTO surface with a dense layer of TiO_2 eliminates access of the monomer to that interface.

presence of the monomer has a negligible effect on the photoelectrochemistry (Figure 6B), except at very positive potentials (>0.6 V vs Ag/AgCl) where the dark anodic current is significant. At more negative potentials, the catalytic effect of the $IrO_x{\cdot}nH_2O$ nanoparticles is negligible, presumably because of the large overpotential for water oxidation by photogenerated holes and the high surface area of the TiO_2 film.

We previously reported that $IrO_x{\cdot}nH_2O$ nanoparticle films could be grown on electrode surfaces through anodization of the monomer solutions.[29] The photoelectrochemistry of such films on rutile-TiO_2 nanorods was studied by depositing $IrO_x{\cdot}nH_2O$ from a 0.5 mM monomer solution for 30 s at +1.0 V vs Ag/AgCl (Figure 6C). The photocurrent was nearly doubled relative to the unmodified electrodes, showing effective catalysis of the OER by electrodeposited $IrO_x{\cdot}nH_2O$. In this case, the surface area of the electrode is low relative to that of mesoporous TiO_2 films, and the catalyst was prepared by direct electrodeposition ensuring good contact to TiO_2. The hydrothermal growth of these nanorods results in a dense 200–400 nm thick TiO_2 underlayer that again physically separates the solution (which may still contain monomeric Ir(III/IV)) from the FTO back-contact.

Taken together, these results suggest that Ir(III/IV) anions mediate electron transfer between electrons trapped at the FTO/TiO_2 interface and holes at the TiO_2 surface, effectively short-circuiting the electrode. We were able to eliminate the possibility that the IrO_x particles themselves act as an electrode shunt by measuring the DC resistance (>2×10^7 Ω) between the FTO back contact and a copper foil contact pressed into the top of the mesoporous TiO_2 film. Therefore, the physical separation of the FTO back contact from the solution is crucial for good photoelectrochemical performance when monomeric Ir(III/IV) anions are present, either in solution or adsorbed to the electrode surface.

We also performed photoelectrochemical experiments on tungsten-doped bismuth vanadate (W–$BiVO_4$) electrodes modified with $IrO_x{\cdot}nH_2O$. Purified PCOOH-capped $IrO_x{\cdot}nH_2O$ colloid solutions were used to deposit the nanoparticles onto the photoanodes. Under these conditions, the photocurrent was enhanced relative to the unmodified W–$BiVO_4$ photoanode, especially at low overpotential (Figure 7A).

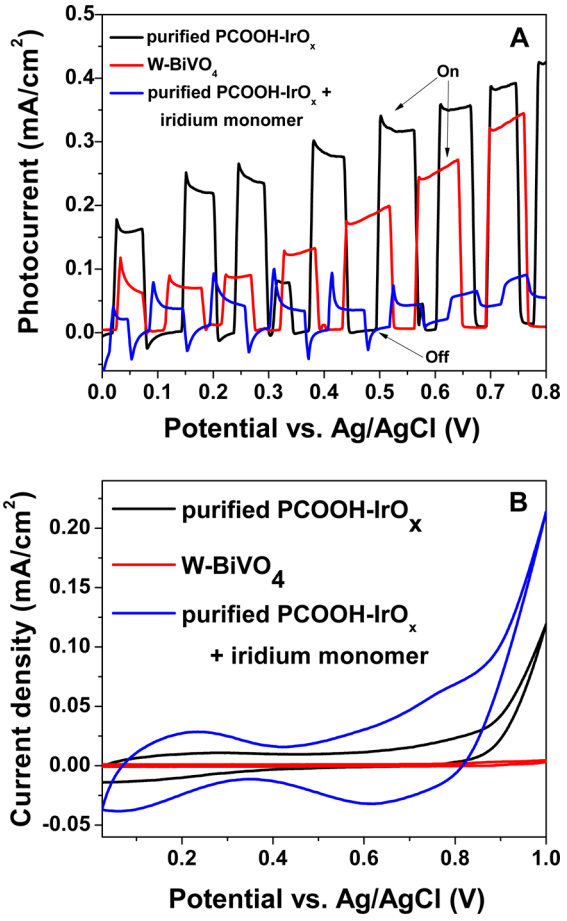

Figure 7. (A) Linear sweep voltammograms (LSV) at 10 mV/s in 0.2 M phosphate buffer (pH 6.8) under AM1.5 irradiation of W–$BiVO_4$ photoelectrodes: (red) bare W–$BiVO_4$, (black) W–$BiVO_4$ electrodes modified with purified PCOOH-capped $IrO_x{\cdot}nH_2O$, and (blue) the same electrode as in the black trace dipped in 1 mM Ir(III/IV) solution for 30 s. (B) Cyclic voltammograms recorded in the dark at 10 mV/s in 0.2 M phosphate buffer (pH 6.8) of bare W–$BiVO_4$ (red), W–$BiVO_4$ modified with purified PCOOH-capped $IrO_x{\cdot}nH_2O$ (black), and the same electrode as the black trace dipped in 1 mM Ir(III/IV) solution for 30 s (blue).

However, when this modified electrode was dipped into a 1 mM Ir(III/IV) monomer solution for 30 s, the photocurrent was dramatically reduced. This is consistent with the observations of the TiO_2 electrodes, namely, that the monomer can effectively short-circuit the system. In addition, dark cyclic voltammograms (Figure 7B, blue trace) show a significant increase in Ir(III/IV) redox peaks after exposure to the monomer solution. This is further proof that the monomer strongly adsorbs and also penetrates the porous electrode to the FTO back contact. This suggests that if a dense W–$BiVO_4$ layer is used, similar to that in the rutile-TiO_2 nanorod or nanostructured hematite electrodes, it is likely that the presence of monomer will not degrade the photoelectrochemical performance of the system.

CONCLUSIONS

In summary, monomeric Ir(III/IV) anions strongly adsorb to the surface of metal oxide photoelectrodes and promote the deposition of $IrO_x{\cdot}nH_2O$ nanoparticles. However, the monomer is detrimental to the performance of photoanodes in water splitting systems based on $IrO_x{\cdot}nH_2O$ catalysis. Enhanced

DOI: 10.1021/jacs.5b03470
J. Am. Chem. Soc. 2015, 137, 8749–8757

photoelectrochemical performance can be attained by using ligand-capped $IrO_x \cdot nH_2O$ catalyst particles that are purified to remove monomeric anions or by using a blocking layer that restricts access of the monomeric anions to the interface between the oxide semiconductor and the electrode back contact.

■ ASSOCIATED CONTENT

Supporting Information

Simulated TDDFT spectra of Ir(III/IV) complexes and raw spectroelectrochemical data. The Supporting Information is available free of charge on the ACS Publications website at DOI: 10.1021/jacs.5b03470.

■ AUTHOR INFORMATION

Corresponding Authors

*jensen@chem.psu.edu
*tem5@psu.edu

Present Addresses

[¶]T.P.S.: Department of Chemistry, University of Wisconsin-Madison, Madison, WI 53706, USA.
[§]J.R.S.: Joint Center for Artificial Photosynthesis and Materials Science Division, Lawrence Berkeley National Laboratory, Berkeley, CA 94720, USA.

Author Contributions

[⊥]Y.Z. and N.M.V.-B. contributed equally.

Notes

The authors declare no competing financial interest.

■ ACKNOWLEDGMENTS

This work was supported by the Office of Basic Energy Sciences, Division of Chemical Sciences, Geosciences, and Energy Biosciences, Department of Energy, under Contract DE-FG02-07ER15911. N.S.M., M.E.S., and N.M.V-B. thank the National Science Foundation for support as graduate fellows under Grant DGE1255832. Y.Z. gratefully acknowledges support of the National Science Foundation of China (Grant No. 21303103).

■ REFERENCES

(1) Nakagawa, T.; Beasley, C.; Murray, R. *J. Phys. Chem. C* **2009**, *113*, 12958.
(2) Zhao, Y.; Hernandez-Pagan, E. A.; Vargas-Barbosa, N. M.; Dysart, J. L.; Mallouk, T. E. *J. Phys. Chem. Lett.* **2011**, *2*, 402.
(3) Yeo, R. S.; Orehotsky, J.; Visscher, W.; Srinivasan, S. *J. Electrochem. Soc.* **1981**, *128*, 1900.
(4) Iwakura, C.; Hirao, K.; Tamura, H. *Electrochim. Acta* **1977**, *22*, 329.
(5) Chen, G. Y.; Delafuente, D. A.; Sarangapani, S.; Mallouk, T. E. *Catal. Today* **2001**, *67*, 341.
(6) Harriman, A.; Thomas, J. M.; Milward, G. R. *New J. Chem.* **1987**, *11*, 757.
(7) Harriman, A.; Pickering, I. J.; Thomas, J. M.; Christensen, P. A. *J. Chem. Soc., Faraday Trans. 1* **1988**, *84*, 2795.
(8) Kanan, M. W.; Nocera, D. G. *Science* **2008**, *321*, 1072.
(9) Huynh, M.; Bediako, D. K.; Nocera, D. G. *J. Am. Chem. Soc.* **2014**, *136*, 6002.
(10) Dincă, M.; Surendranath, Y.; Nocera, D. G. *Proc. Natl. Acad. Sci. U. S. A.* **2010**, *107*, 10337.
(11) Gorlin, Y.; Jaramillo, T. F. *J. Am. Chem. Soc.* **2010**, *132*, 13612.
(12) McCrory, C. C. L.; Jung, S.; Peters, J. C.; Jaramillo, T. F. *J. Am. Chem. Soc.* **2013**, *135*, 16977.
(13) Louie, M. W.; Bell, A. T. *J. Am. Chem. Soc.* **2013**, *135*, 12329.
(14) Trotochaud, L.; Young, S. L.; Ranney, J. K.; Boettcher, S. W. *J. Am. Chem. Soc.* **2014**, *136*, 6744.
(15) Tilley, S. D.; Cornuz, M.; Sivula, K.; Grätzel, M. *Angew. Chem., Int. Ed.* **2010**, *49*, 6405.
(16) Zhong, D. K.; Gamelin, D. R. *J. Am. Chem. Soc.* **2010**, *132*, 4202.
(17) Zhong, D. K.; Choi, S.; Gamelin, D. R. *J. Am. Chem. Soc.* **2011**, *133*, 18370.
(18) Lin, F.; Boettcher, S. W. *Nat. Mater.* **2013**, *13*, 81.
(19) Kleiman-Shwarsctein, A.; Hu, Y.; Forman, A.; Stucky, G.; McFarland, E. *J. Phys. Chem. C* **2008**, *112*, 15900.
(20) Bornoz, P.; Abdi, F. F.; Tilley, S. D.; Dam, B.; van de Krol, R.; Grätzel, M.; Sivula, K. *J. Phys. Chem. C* **2014**, *118*, 16959.
(21) Abdi, F. F.; van de Krol, R. *J. Phys. Chem. C* **2012**, *116*, 9398.
(22) Badia-Bou, L.; Mas-Marza, E.; Rodenas, P.; Barea, E. M.; Fabregat-Santiago, F.; Gimenez, S.; Peris, E.; Bisquert, J. *J. Phys. Chem. C* **2013**, *117*, 3826.
(23) Bledowski, M.; Wang, L.; Neubert, S.; Mitoraj, D.; Beranek, R. *J. Phys. Chem. C* **2014**, *118*, 18951.
(24) Abe, R.; Higashi, M.; Domen, K. *J. Am. Chem. Soc.* **2010**, *132*, 11828.
(25) Maeda, K.; Higashi, M.; Siritanaratkul, B.; Abe, R.; Domen, K. *J. Am. Chem. Soc.* **2011**, *133*, 12334.
(26) Ye, H.; Lee, J.; Jang, J. S.; Bard, A. J. *J. Phys. Chem. C* **2010**, *114*, 13322.
(27) Ye, H.; Park, H. S.; Bard, A. J. *J. Phys. Chem. C* **2011**, *115*, 12464.
(28) Zhao, Y.; Swierk, J. R.; Megiatto, J. D.; Sherman, B.; Youngblood, W. J.; Qin, D.; Lentz, D. M.; Moore, A. L.; Moore, T. A.; Gust, D.; Mallouk, T. E. *Proc. Natl. Acad. Sci. U. S. A.* **2012**, *109*, 15612.
(29) Zhao, Y.; Vargas-Barbosa, N. M.; Hernandez-Pagan, E. A.; Mallouk, T. E. *Small* **2011**, *7*, 2087.
(30) Lee, S.-H. A.; Abrams, N. M.; Hoertz, P. G.; Barber, G. D.; Halaoui, L. I.; Mallouk, T. E. *J. Phys. Chem. B* **2008**, *112*, 14415.
(31) Liu, B.; Aydil, E. S. *J. Am. Chem. Soc.* **2009**, *131*, 3985.
(32) te Velde, G.; Bickelhaupt, F. M.; Baerends, E. J.; Fonseca Guerra, C.; van Gisbergen, S. J. A.; Snijders, J. G.; Ziegler, T. *J. Comput. Chem.* **2001**, *22*, 931.
(33) Fonseca Guerra, C.; Snijders, J. G.; te Velde, G.; Baerends, E. J. *Theor. Chem. Acc.* **1998**, *99*, 391.
(34) Baerends, E.; Ziegler, T.; Autschbach, J.; Bashford, D.; Bérces, A.; Bickelhaupt, F.; Bo, C.; Boerrigter, P.; Cavallo, L.; Chong, D.; Deng, L.; Dickson, R.; Ellis, D.; van Faassen, M.; Fan, L.; Fischer, T.; Guerra, C. F.; Franchini, M.; Ghysels, A.; Giammona, A.; van Gisbergen, S.; Götz, A.; Groeneveld, J.; Gritsenko, O.; Grüning, M.; Gusarov, S.; Harris, F.; van den Hoek, P.; Jacob, C.; Jacobsen, H.; Jensen, L.; Kaminski, J.; van Kessel, G.; Kootstra, F.; Kovalenko, A.; Krykunov, M.; van Lenthe, E.; McCormack, D.; Michalak, A.; Mitoraj, M.; Morton, S.; Neugebauer, J.; Nicu, V.; Noodleman, L.; Osinga, V.; Patchkovskii, S.; Pavanello, M.; Phillipsen, P.; Post, D.; Pye, C.; Ravenek, W.; Rodríguez, J.; Ros, P.; Schipper, P.; Scheckenbach, G.; Seldenthuis, J.; Seth, M.; Snijders, J.; Solá, M.; Swart, M.; Swerhone, D.; Velde, te, G.; Vernooijs, P.; Verluis, L.; Visscher, L.; Visser, O.; Wang, F.; Wesolowski, T.; van Wezenbeek, E.; Weisenekker, G.; Wolff, S.; Woo, T.; Yakovlev, A. ADF2014, SCM, Theoretical Chemistry, Vrije Universiteit, Amsterdam, The Netherlands.
(35) Swart, M.; Ehlers, A. W.; Lammertsma, K. *Mol. Phys.* **2007**, *102*, 2467.
(36) Klamt, A.; Schüürmann, G. *J. Chem. Soc., Perkin Trans. 2* **1993**, 799.
(37) van Lenthe, E.; Baerends, E. J.; Snijders, J. G. *J. Chem. Phys.* **1993**, *99*, 4597.
(38) van Lenthe, E.; Baerends, E. J.; Snijders, J. G. *J. Chem. Phys.* **1994**, *101*, 9783.
(39) Seth, M.; Ziegler, T. *J. Chem. Theory Comput.* **2012**, *8*, 901.
(40) Nahor, G. S.; Hapiot, P.; Neta, P.; Harriman, A. *J. Phys. Chem.* **1991**, *95*, 616.
(41) Harriman, A.; Nahor, G. S.; Mosseri, S.; Neta, P. *J. Chem. Soc., Faraday Trans. 1* **1988**, *84*, 2821.

DOI: 10.1021/jacs.5b03470
J. Am. Chem. Soc. 2015, 137, 8749−8757

(42) Beutler, P.; Gamsjäger, H. *J. Chem. Soc., Chem. Commun.* **1976**, 554.
(43) Castillo-Blum, S. E.; Richens, D. T.; Sykes, A. G. *J. Chem. Soc., Chem. Commun.* **1986**, 1120.
(44) Pankratov, D. A.; Komozin, P. N.; Kiselev, Y. M. *Russ. J. Inorg. Chem.* **2011**, *56*, 1794.
(45) Blakemore, J. D.; Schley, N. D.; Kushner-Lenhoff, M. N.; Winter, A. M.; D'Souza, F.; Crabtree, R. H.; Brudvig, G. W. *Inorg. Chem.* **2012**, *51*, 7749.
(46) Hintermair, U.; Hashmi, S. M.; Elimelech, M.; Crabtree, R. H. *J. Am. Chem. Soc.* **2012**, *134*, 9785.
(47) Fine, D. A. *Inorg. Chem.* **1969**, *8*, 1014.
(48) Cady, H. H.; Connick, R. E. *J. Am. Chem. Soc.* **1958**, *80*, 2646.
(49) Baur, J. E.; Spaine, T. W. *J. Electroanal. Chem.* **1998**, *443*, 208.
(50) Eisenberg, D.; Ahn, H. S.; Bard, A. J. *J. Am. Chem. Soc.* **2014**, *136*, 14011.

DOI: 10.1021/jacs.5b03470
J. Am. Chem. Soc. 2015, 137, 8749−8757